ACS Catalysis

pubs.acs.org/acscatalysis

Research Article

# Role of Defects in the Interplay between Adsorbate Evolving and Lattice Oxygen Mechanisms of the Oxygen Evolution Reaction in $RuO_2$ and $IrO_2$

Alexandra Zagalskaya and Vitaly Alexandrov*

Cite This: *ACS Catal.* 2020, 10, 3650−3657

Read Online

ACCESS | Metrics & More | Article Recommendations | Supporting Information

**ABSTRACT:** The mechanistic interplay between the oxygen evolution reaction (OER) and material degradation during water electrolysis is not yet well understood even for the most studied OER electrocatalysts such as $RuO_2$ and $IrO_2$. It is still disputed whether the lattice oxygen mechanism (LOM) may be competitive with the conventional adsorbate evolving mechanism (AEM) of the OER in these materials and, if so, under what conditions. Herein, we employ density functional theory calculations to demonstrate that the LOM can give rise to higher OER activity than the AEM at the active sites involving structural defects, both intrinsic and extrinsic. Specifically, we show that, although the AEM is preferred for the perfect (110) and (211) surfaces, the formation of metal vacancies due to catalyst dissolution may lead to much lower OER overpotentials for the LOM. Also, by screening several metal impurities in $RuO_2$, we reveal that dopants such as Ni and Co can promote the LOM over the AEM even for the perfectly structured surfaces. Overall, we demonstrate that defective $IrO_2$ is less LOM active than $RuO_2$ that should contribute to its superior stability under OER conditions.

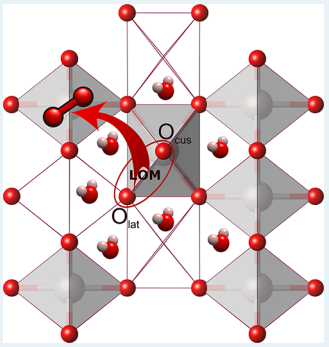


**KEYWORDS:** *density functional theory, lattice oxygen mechanism, oxygen evolution reaction, rutile, electrocatalysis*



## INTRODUCTION

Water electrolysis ($H_2O \rightarrow H_2 + O_2$) is an attractive way to store energy from renewable sources in the form of clean hydrogen.[1−5] The four-electron oxygen evolution reaction (OER) at the anode ($2H_2O \rightarrow O_2 + 4H^+ + 4e^-$) exhibits more sluggish kinetics than the two-electron hydrogen evolution reaction (HER) at the cathode ($2H^+ + 2e^- \rightarrow H_2$).[6] Consequently, the oxidative half-cell reaction (OER) has been the emphasis of a lot of theoretical and experimental studies aimed to develop electrocatalysts with improved OER activity.[7,8] Despite the scarcity and high cost, rutile-structured $RuO_2$ and $IrO_2$ catalysts remain benchmark OER anodes due to their favorable combination of activity/stability characteristics.[9,10]

Mechanistically, a number of reaction pathways have been proposed in the literature for the OER in metal-oxide catalysts. According to the conventional adsorbate evolving mechanism (AEM), surface metal-ion centers serve as catalytically active sites on which $H_2O$ molecules from solution undergo the four concerted proton-electron transfer steps to yield $O_2$ (see Figure 1). However, this mechanism has been challenged in a series of experimental studies revealing that oxygen may also evolve from the oxide.[11−15] For example, in a recent experimental investigation utilizing in situ $^{18}O$ isotope labeling mass spectrometry, it has been directly demonstrated that $O_2$ can be generated from lattice oxygen in perovskites such as $SrCoO_{3-\delta}$, $La_{0.5}Sr_{0.5}CoO_{3-\delta}$, and $Pr_{0.5}Ba_{0.5}CoO_{3-\delta}$.[13] The reason for the lattice oxygen activation was shown to be the greater covalency of the metal-oxygen bonds that can be quantified by estimating charge transfer gap between metal 3d and oxygen 2p states. Recently, multiple density functional theory (DFT) studies have shown that the LOM can indeed deliver higher OER activity than the conventional AEM in various oxide catalysts such as $ABO_3$ (A = alkaline earth, B = transition metal) perovskites[13,16] and MOOH metal oxyhydroxides.[17]

Contrary to the perovskite materials, the lattice oxygen participation in the OER for rutile-structured electrocatalysts such as $RuO_2$ and $IrO_2$ is still debated. It was experimentally observed for nanocrystalline $RuO_2$-based catalysts that the involvement of lattice oxygen in the OER becomes pronounced at potentials above 1.12 V.[12] Specifically, it was detected that the contribution of the oxygen exchange mechanism could reach 50% of the total oxygen for $Ru_{0.9}Ni_{0.1}O_{2-\delta}$ and approximately 9% for pure $RuO_2$. However, a recent experimental study showed no evidence of oxygen exchange on the regular $RuO_2$ (100), (110), (101), and (111) surfaces in both basic and acidic environments.[18] Therefore, it

Received: December 23, 2019
Revised: February 20, 2020
Published: February 21, 2020





https://dx.doi.org/10.1021/acscatal.9b05544
*ACS Catal.* 2020, 10, 3650−3657

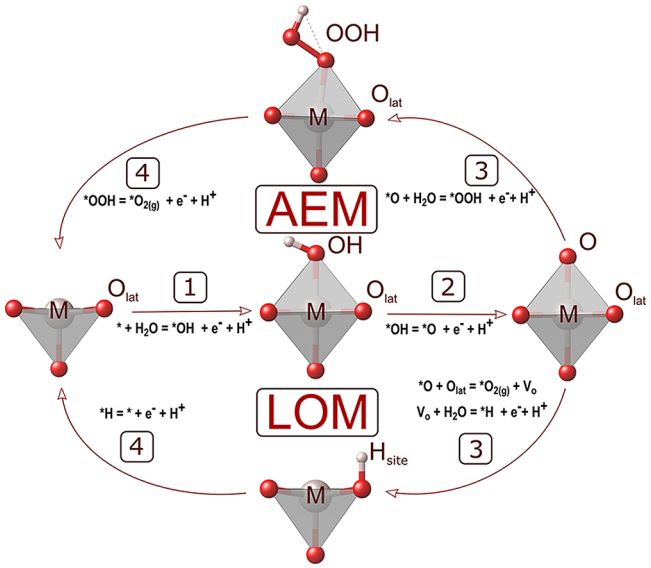


**Figure 1.** Schematic representation of the adsorbate evolving mechanism (AEM) and lattice oxygen mechanism (LOM) considered in this study. The four electrochemical reaction steps for each mechanism are shown with "*" and $V_O$ denoting bare surface and lattice oxygen vacancy, respectively. M stands for metal (Ru, Ir).

could be hypothesized that the discrepancy between the two sets of experimental results may be due to different chemistries of the surface active sites and surface crystallinity of the used catalysts.

In addition to structural differences between the oriented films and their nanocrystalline analogues, the OER mechanism and kinetics also depend on the structural evolution of nanocatalysts under dynamic OER working conditions.[19−24] For example, it was recently demonstrated computationally that, even at potentials much lower than the OER onset, $RuO_2$ and $IrO_2$ nanoparticles should undergo substantial morphological/compositional transformations affecting their OER activity.[25] Such surface reconstruction processes are also expected to be coupled to metal dissolution since it is established that the onsets of the OER and dissolution for $RuO_2$ and $IrO_2$ catalysts coincide well.[9,26] In fact, we have recently demonstrated that $RuO_2$ dissolution intermediates can greatly lower the theoretical OER overpotential.[22] Thus, we may hypothesize that the experimental observation of a more pronounced involvement of the LOM to the OER at higher potentials[12] could be also related to the presence of metal vacancies formed during catalyst dissolution.

Based on this prior knowledge, we set out to answer the following questions in this study: (i) Can the presence of defect sites, such as metal dopants like in $Ru_{0.9}Ni_{0.1}O_{2-\delta}$ and/or metal vacancies formed during metal-oxide dissolution, favor the LOM over the AEM? If yes, (ii) is it $RuO_2$ or $IrO_2$ that is more LOM active? The latter question is directly related to the stability issue, namely, whether the difference in LOM activity between these two oxides can contribute to the exceptional stability of $IrO_2$-based catalysts.

## COMPUTATIONAL METHODOLOGY

Spin-polarized DFT calculations were performed using the Vienna Ab Initio Simulation Package (VASP).[27,28] The revised Perdew−Burke−Ernzerhof (RPBE) functional[29,30] along with Grimme's D3-dispersion correction[31,32] to take into account long-range van der Waals interactions were employed. Ionic cores of all atoms were described using projector augmented wave (PAW) pseudopotentials[33,34] from the VASP library (PAW_PBE Ru, Ir, O, H, Ni_pv, Co_pv, Fe_pv, Mn_pv, and Cr_pv). A plane-wave cutoff energy of 400 eV was used.

The lattice parameters of the rutile structure were optimized to give $a$ = 4.543 Å, $c$ = 3.140 Å for $RuO_2$, and $a$ = 4.545 Å, $c$ = 3.190 Å for $IrO_2$. Periodic slab models of the $MO_2$(110) and $MO_2$(211) (M = Ru, Ir) surfaces were constructed in VESTA[35] using 2 × 3 and 2 × 2 surface supercells, correspondingly, with four metal-oxide layers separated by at least 10 Å vacuum gap, resulting in the same chemical composition of $M_{48}O_{96}$. These (110) and (211) surfaces were chosen for modeling to represent low- and high-energy facets, respectively, that can be observed experimentally for nanocrystalline rutile oxides.[36,37] The bottom layer of each slab was fixed to the bulk positions, while the top three layers were allowed to relax until the atomic forces became less than 0.05 eV/Å. For the structures involving metal-ion vacancies, the changes in cell volume with respect to perfect structures were taken into account by re-optimizing geometries prior to OER calculations. A 3 × 4 × 1 Monkhorst-Pack sampling of reciprocal space was used in all slab calculations. DFT-computed surface energies for the ideal (110) and (211) facets are 1.43 and 2.41 J/m$^2$ for $RuO_2$ and 1.88 and 3.10 J/m$^2$ for $IrO_2$, respectively, in good agreement with previous theoretical estimates.[36,38] For the systems involving substitutional dopants, the rotationally invariant version of the DFT+$U$ approach[39−42] was used with the on-site Coulomb interaction parameters of 3.5, 3.9, 5.0, 3.3, and 6.45 eV for Cr, Mn, Fe, Co, and Ni, respectively, adopted from a previous study.[43] The choice of the metal dopants was motivated by previous experimental and theoretical studies of complex metal oxides[12,15,16,37] allowing us to systematically analyze their effect on the OER.

The computational hydrogen electrode (CHE) approach was employed to evaluate OER thermodynamic overpotentials.[44,45] The Gibbs free energies for the OER were calculated including zero-point energy (ZPE) and vibrational entropy $S_{vib}$ corrections taken from previous studies[22,45,46] as 0.36, 0.07, 0.40, and 0.28 eV for *OH, *O, *OOH, and $*H_{O-site}$, respectively, independent of the $MO_2$ system. We decided not to include implicit solvent effects in our calculations as it is unclear what dielectric constant should be used for the complex interfaces involving defects. Nevertheless, our test calculations for $RuO_2$ using the VASPsol implementation of the implicit solvent model[47] indicated that the observed trend (the decrease in the OER overpotential for both the AEM and LOM making the LOM competitive with the AEM for the defective systems) is preserved.

## RESULTS AND DISCUSSION

Figure 1 illustrates the conventional adsorbate evolving mechanism (AEM) versus lattice-oxygen participation mechanism (LOM) of the OER, the competition between which has been widely discussed in the literature.[15] In this work, we examine the interplay between these two mechanisms for $RuO_2$- and $IrO_2$-based catalysts. First, we discuss the results obtained for the regular (non-defective) $MO_2$(110) and (211) facets showing that such ideal surfaces are characterized by greater OER activity for the AEM, in agreement with previous experiments and DFT calculations. Second, we contrast the two mechanisms in the case of transition metal-doped $MO_2$


https://dx.doi.org/10.1021/acscatal.9b05544
ACS Catal. 2020, 10, 3650−3657

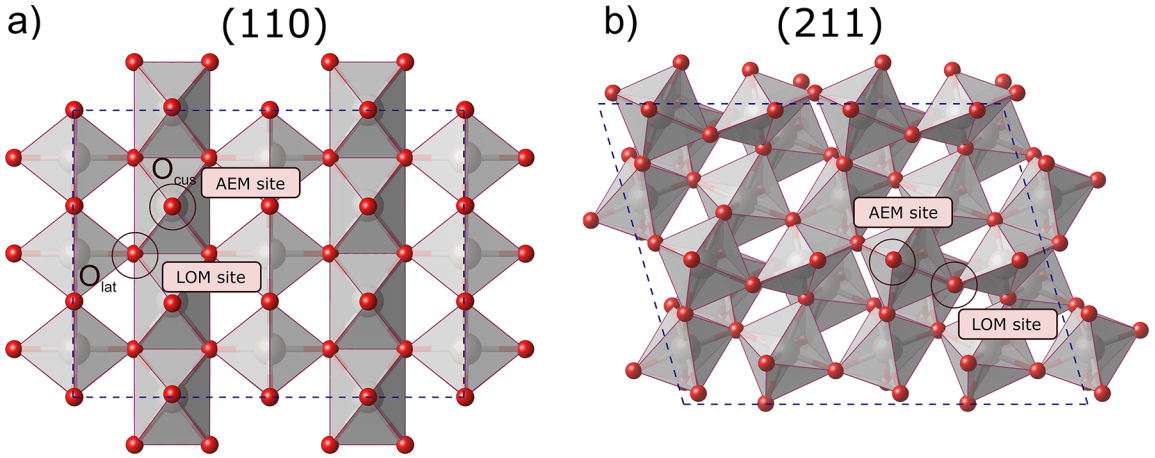


**Figure 2.** Top view of (a) (110) and (b) (211) surfaces of rutile-structured $RuO_2$ and $IrO_2$ employed in DFT calculations of the OER overpotentials. $O_{cus}$ and $O_{lat}$ denote the active sites on which the AEM and LOM are examined, respectively.

demonstrating that certain substitutional dopants can indeed switch the OER mechanism from the AEM to LOM. Third, we compare the OER behavior of the surface active sites in the presence of metal-ion vacancies formed upon dissolution and reveal that such defect sites may also favor the LOM over the AEM. Furthermore, we demonstrate that the synergetic effect in facilitating the LOM over the AEM can be achieved in the presence of both types of defects (dopants and vacancies). Finally, we correlate the calculated overpotentials for the AEM and LOM with the transition metal 3d and oxygen 2p band centers that helps explain why the LOM becomes a more favorable mechanism of the OER.

**Ideal $MO_2$ (M = Ru, Ir) (110) and (211) Surfaces.** It was discussed above that polycrystalline films or nanoparticles of rutile catalysts exhibit different OER activities than regular low-index surfaces.[12,15,18] Therefore, we first compare the reaction thermodynamics for both OER mechanisms at the ideal fully oxidized $MO_2$(110) and (211) facets chosen here to represent the low- and high-index rutile surfaces (see Figure 2). The OER proceeds at the coordinatively undersaturated site ($O_{cus}$) in the case of the AEM and at the lattice site ($O_{lat}$) in the case of the LOM according to the reaction pathways depicted in Figure 1. The DFT-based free energy diagrams for the OER via the AEM and LOM for the $RuO_2$ and $IrO_2$ surfaces are presented in Figures 3 and 4. It is seen from the diagrams that the theoretical OER overpotential is always much higher for the LOM ($\eta_{LOM}$) than AEM ($\eta_{AEM}$). It is interesting to note that the higher-energy (211) facet of $IrO_2$ appears to exhibit lower AEM and LOM overpotentials than (110). Overall, our OER overpotentials calculated for the AEM are in good

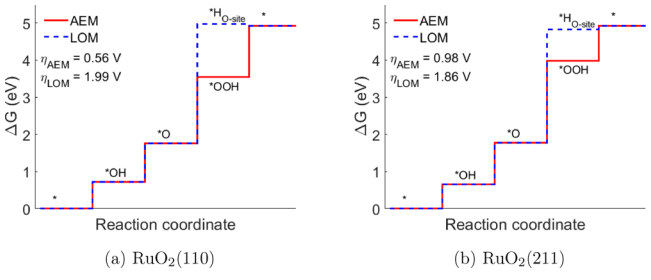


**Figure 3.** Free energy diagrams for OER via AEM (red solid line) and LOM (blue dashed line) for (a) $RuO_2$(110) and (b) $RuO_2$(211).

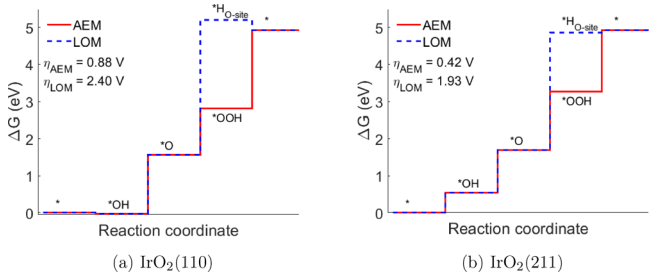


**Figure 4.** Free energy diagrams for OER via AEM (red solid line) and LOM (blue dashed line) for (a) $IrO_2$(110) and (b) $IrO_2$(211).

agreement with previous theoretical investigations[48−50] as seen from Table S1.

**Substitutional Metal Dopants at $RuO_2$ Surfaces.** We next proceed to examine the influence of structural defects on OER activity. In this section, we focus on substitutional transition metal dopants (Ni, Co, Cr, Fe, and Mn) considering as an example the $RuO_2$(110) and (211) surfaces. Figure 5

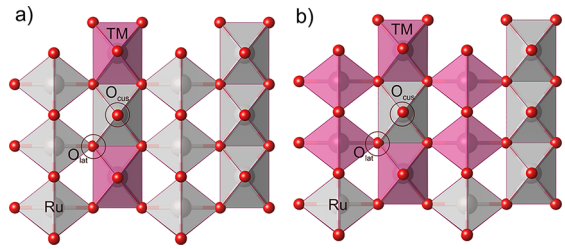


**Figure 5.** Top view of the transition metal (TM)-doped $RuO_2$(110) surface: (a) two $M_{cus}$ are substituted by a transition metal dopant, and (b) six TM sites are substituted by a transition metal dopant corresponding to 16.7 and 50% dopant concentrations at the surface, respectively.

shows two structural models adopted here to investigate the role of dopants corresponding to two different surface concentrations (16.7 and 50%). Since it is expected that the highest dopant concentration (with six surface dopants, Figure 5b) should lead to the most pronounced effect on OER overpotentials, we first screen doped systems at this concentration by looking at the non-oxidized $RuO_2$(110) surface (see Table S2). We find that, in all cases, the third


https://dx.doi.org/10.1021/acscatal.9b05544
ACS Catal. 2020, 10, 3650−3657

electrochemical step (see the scheme in Figure 1) is potential-determining, similarly to the non-doped rutile surfaces. It is seen that the OER overpotential increases for AEM and decreases for the LOM upon doping. Importantly, in the case of six dopants for Ni and Co, the LOM exhibits higher OER activity than the AEM. It turns out that the presence of only two surface dopants is not enough to switch from the AEM to LOM (Table S2).

We observe exactly the same situation for the oxidized $RuO_2(110)$ surface, and Figure 6 shows the free energy

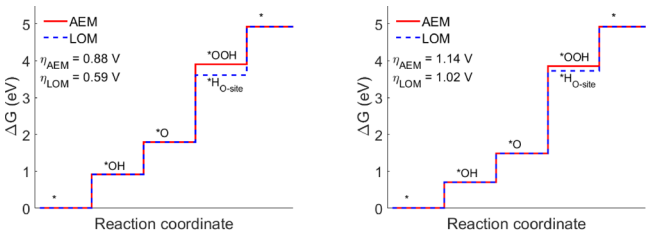


(a) 6-Ni-$RuO_2$(110) (b) 6-Co-$RuO_2$(110)

**Figure 6.** Free energy diagrams for OER via AEM (red solid line) and LOM (blue dashed line) for (a) doped $RuO_2(110)$ with six Ni atoms and (b) doped $RuO_2(110)$ with six Co atoms.

diagrams for Ni and Co. For both non-oxidized and oxidized $RuO_2(110)$, we observe that Ni has a more profound effect than Co on the difference between $\eta_{LOM}$ and $\eta_{AEM}$. Thus, we demonstrate that, even for the regular $RuO_2(110)$ surface with dopants, there should be a crossover between the two OER mechanisms, and we expect a similar behavior for other facets. This result is in agreement with experimental findings of lattice oxygen exchange that was detected to be significantly higher for $Ru_{0.9}Ni_{0.1}O_{2-\delta}$ than pure $RuO_2$.[12] We also find that this OER behavior can be related to the electronic structure of the active $O_{cus}$ and $O_{lat}$ sites, as will be discussed below.

**Metal Vacancies at $MO_2$ Surfaces.** We next turn to the analysis of metal-ion vacancies that can be formed at the surface throughout the dissolution process and discuss their influence on the OER. It is established experimentally that instability of $RuO_2$ and $IrO_2$ catalysts can be linked to the electrochemical OER process since the onsets of the OER and dissolution coincide well. As a result, unstable species such as $RuO_4$ and $IrO_3$ are formed, leaving behind the metal-ion vacancies at the surface and triggering the formation of highly OER active amorphous hydrous layers.[9,23,51] Recently, we have demonstrated that metastable surface-bound dissolution intermediates can indeed lower the OER overpotential as compared with regular rutile surfaces.[22] For the purpose of this study, we now analyze how metal vacancies left behind during catalyst dissolution can affect the OER activity via the AEM and LOM. We discuss first the systems involving only metal vacancies and then extend our study to include models in which both substitutional dopants and metal vacancies are present. This allows us to analyze the combined effect brought out by these defects on the OER activity.

Figure 7 shows several structural models for the (110) surface adopted in this study involving one, two, and three metal vacancies with the AEM and LOM sites denoted as $O_{cus}$ and $O_{lat}$, respectively. The corresponding OER overpotentials derived from DFT are listed in Table 1. It is seen from the table that the presence of metal vacancies has a marked effect on the OER activity. In the case of $RuO_2$, the observed effect is

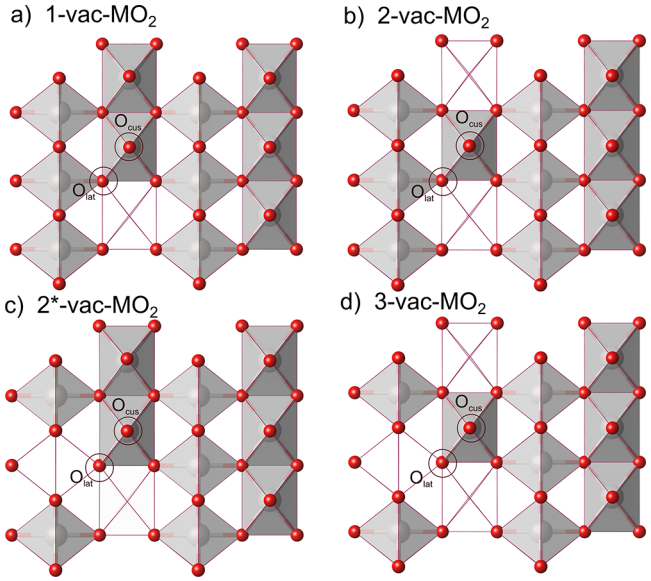


**Figure 7.** (a–d) Top view of the structural models for $MO_2(110)$ (M = Ru, Ir) containing one, two, and three M vacancies. White polyhedra depict the positions of vacancies.

**Table 1. Computed OER Overpotentials (in V) via AEM and LOM at the $MO_2(110)$ (M = Ru, Ir) Surface with Zero to Three M Vacancies, where Structural Models Are Shown in Figure 7[a]**

| system | mechanism | regular | 1-vac | 2-vac | 2*-vac | 3-vac |
|---|---|---|---|---|---|---|
| $RuO_2$ (110) | AEM | 0.56 | 0.43 | 0.16 | 0.39 | 0.23 |
| | LOM | 1.99 | 0.87 | 0.16 | 0.64 | 0.20 |
| $IrO_2$ (110) | AEM | 0.88 | 0.70 | 0.38 | 0.30 | 0.27 |
| | LOM | 2.40 | 1.19 | 0.81 | 0.59 | 0.33 |

[a]The corresponding Gibbs free energies are listed in Table S3.

similar to substitutional dopants as vacancies lead not only to decreased OER overpotentials but also to rendering the LOM competitive with the AEM. It is also interesting to note that the effect of removing Ru ions from the two cus positions (2-vac-$MO_2$ model, Figure 7b) is more pronounced than creating one vacancy at the bridge and the second one at the cus site (2*-vac-$MO_2$ model, Figure 7c). In the case of $IrO_2(110)$, however, we observe that the AEM still displays greater OER activity than the LOM for all defective models considered.

A similar situation can be observed when comparing the OER behavior of the $RuO_2$ and $IrO_2(211)$ surfaces containing metal vacancies. Specifically, we can see from the free energy diagrams in Figures 8 and 9 that two surface vacancies can switch the AEM to a more favorable LOM for $RuO_2$, but not for $IrO_2$. We can thus conclude that $IrO_2$ appears to be less active toward the LOM. Since the degree of lattice oxygen participation in the OER can be correlated with the lattice instability,[23] we can suggest that lower LOM activity of $IrO_2$ can also contribute to its superior stability as compared with $RuO_2$.

**Combination of Two Defect Types at the Surface.** Further, we also analyze the presence of both types of structural defects, transition metal dopants, and metal vacancies, revealing their synergistic effect on the OER. Since the high dopant content at the surface considered above may not be highly probable experimentally for doped $MO_2$, we focus here on the cases of small defect concentrations at the


https://dx.doi.org/10.1021/acscatal.9b05544
ACS Catal. 2020, 10, 3650−3657

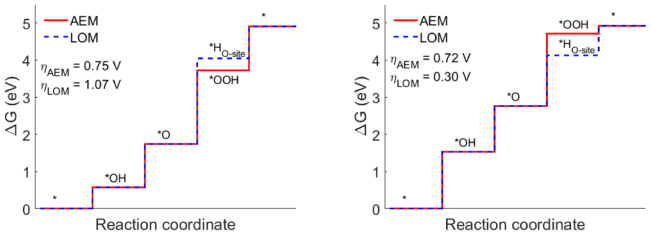


(a) 1-vac-$RuO_2$(211) (b) 2-vac-$RuO_2$(211)

**Figure 8.** Free energy diagrams for OER via AEM (red solid line) and LOM (blue dashed line) for $RuO_2$(211) with (a) one Ru vacancy and (b) two Ru vacancies.

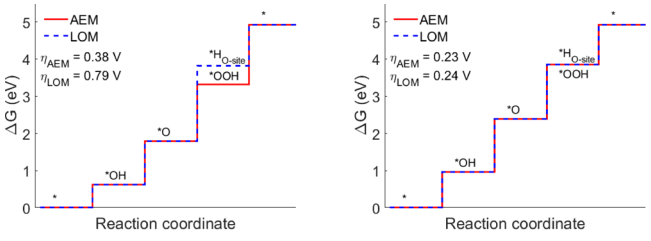


(a) 1-vac-$IrO_2$(211) (b) 2-vac-$IrO_2$(211)

**Figure 9.** Free energy diagrams for OER via AEM (red solid line) and LOM (blue dashed line) for $IrO_2$(211) with (a) one Ir vacancy and (b) two Ir vacancies.

surface by analyzing combinations of one or two Ni dopants with one or two metal vacancies on the example of the $RuO_2$(110) surface. As we determine a clear correlation between the OER activity and O 2p-band center position (see the discussion below), we employ the position of the band center as a descriptor in our computational screening. In doing so, we are able to identify the most promising surface structure combining one Ni atom and two metal vacancies, as illustrated in Figure 10. For this structure, we then perform the OER

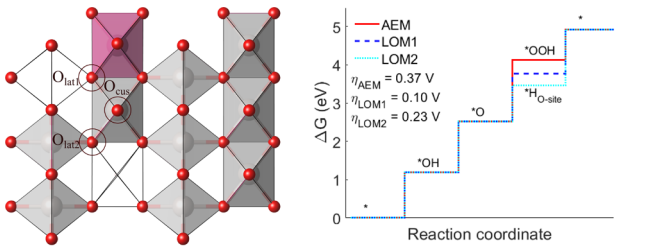


(a) 1-Ni-2*-vac-$RuO_2$(110) (b) Free energy diagrams for 1-Ni-2*-vac-$RuO_2$(110)

**Figure 10.** (a) Structural model of $RuO_2$(110) with two vacancies doped by one Ni atom ("*" designated one bridge and one cus vacancy). (b) Free energy diagrams for AEM (red solid line), LOM1 (blue dashed line), and LOM2 (cyan dotted line).

thermodynamic calculations for both the AEM and LOM and indeed reveal that the LOM becomes more favorable than the AEM (see Figure 10b).

In addition to the situation of a relatively low defect concentration at the surface, we examine the mixed-defect case with five Ni dopants and one metal vacancy as shown in Figure S1. This case is similar to the one involving six Ni dopants at $RuO_2$(110) considered earlier but allows us to further analyze the synergy between two types of defects. It is seen from Table S4 that although AEM is preferred over the LOM in the case of only one Ru vacancy (0.43 V vs 0.87 V), the situation can be completely reversed by adding five substitutional Ni dopants in the vicinity of the reaction site (0.86 V for the AEM vs 0.46 V for the LOM). If we now compare the latter case with the results obtained for six substitutional Ni dopants (see Figure 6a), it can be observed that $\eta_{LOM}$ is lower for the mixed-defect situation (0.46 V vs 0.59 V) showing the synergistic effect of two types of defects at the $RuO_2$(110) surface. These findings for the mixed-defect situations have important implications for the interpretation of the OER activity in materials where both types of defects can be present such as $Ru_{0.9}Ni_{0.1}O_{2-\delta}$.

To even further demonstrate that the phenomenon of switching between the AEM and LOM has a general nature regardless of the chosen atomic-structure model, we also analyze the OER activity at the $RuO_2$(121) double kink (see the structural model in Figure S2). It is believed that kinks should play a dominant role in defining the overall dissolution/nucleation kinetics across a number of materials.[52−54] Previously, the role of $RuO_2$(121) double kinks in the OER was considered in a number of theoretical works in the context of a conventional OER mechanism.[22,50] Here, we extend this analysis by examining the LOM at this model kink site. The pristine kink site (see Table S5) displays an OER overpotential of 0.39 V for the AEM, which is lower than that of the ideal (110) surface.[22,50] However, when the kink is doped by several Ni atoms (see Figure S2), the LOM becomes as thermodynamically favorable as the AEM. Thus, we find the same trend as for other structural models discussed above where, upon doping, $\eta_{AEM}$ increases and $\eta_{LOM}$ decreases, leading to a crossover in OER activity.

**Correlation between the OER Overpotentials and Electronic Properties of Catalytically Active Sites.** To better understand the AEM and LOM at $RuO_2$ and $IrO_2$ surfaces, we investigate the local electronic structure of the $O_{cus}$ and $O_{lat}$ sites using a projected density of states (DOS) analysis. Such analysis has proved to be successful in explaining catalytic activity trends across a variety of catalysts based on electronic-structure descriptors such as transition metal d- and oxygen p-band centers.[13,50,55,56] Specifically, it was shown that the O 2p-band center can serve as a descriptor for the OER activities of perovskites,[55] analogously to the d-band center for metal catalysts. This is because the O 2p band is believed to accurately capture the electronic structure properties of oxides, especially in the context of the OER in which the electrochemical steps occur at the oxygen sites. In the case of the OER, oxidation of oxygen becomes thermodynamically favorable when O 2p states at the materials Fermi level lie above the redox energy of the $O_2/H_2O$ couple. It was demonstrated on the example of perovskites[13] that metal substitution at the A-sublattice of the $ACoO_3$ structure (e.g., $Sr^{2+}$ by $La^{3+}$) can promote participation of lattice oxygen in the OER if the Fermi level moves closer to the O 2p states, leading to the more covalent nature of the metal−oxygen bonds.

Figure 11 shows the calculated DOS projected onto the 2p states of the $O_{lat}$ site participating in the LOM. It can be seen that the O 2p-band center clearly shifts to more positive values (closer to the Fermi level) when going from the ideal (110) to one- and two-vacancy surface models for both $RuO_2$ and $IrO_2$. A similar trend is observed when analyzing DOS for the $O_{cus}$ site involved in the AEM shown in Figure S3. To be able to compare the behavior of two catalysts toward the AEM and LOM, we also plot the computed OER overpotentials versus O 2p-band centers for the three structural models with metal


https://dx.doi.org/10.1021/acscatal.9b05544
ACS Catal. 2020, 10, 3650−3657

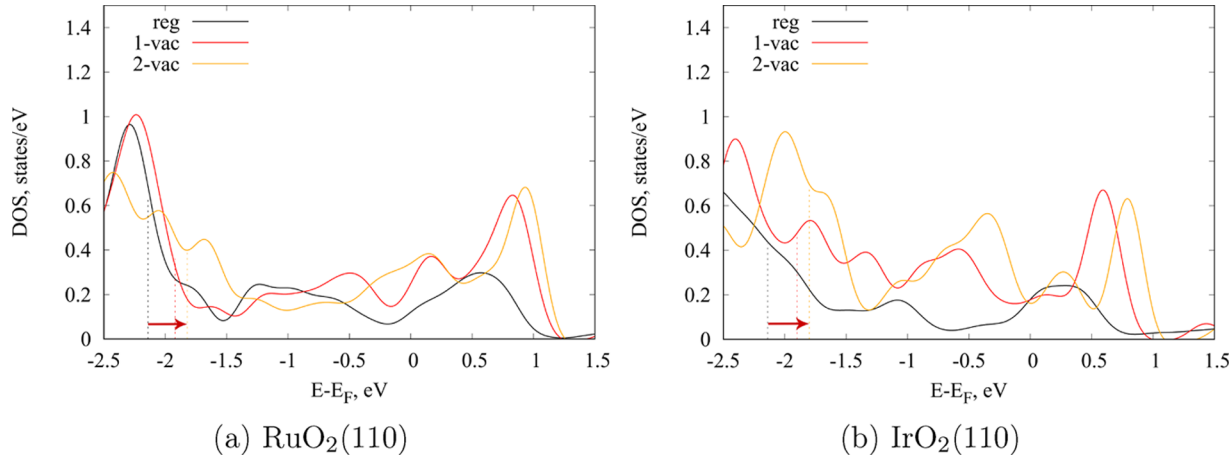


**Figure 11.** Density of states projected onto the 2p states of the $O_{lat}$ site participating in the AEM at (a) $RuO_2$(110) and (b) $IrO_2$(110) for regular (reg), one M (1-vac), and two M (2-vac) vacancies surface models. The positions of the O 2p-band center are indicated by dashed lines, showing a shift closer to the Fermi level (taken as zero) when going from the ideal to defective surfaces. The arrows show the band center displacement.

vacancies (Figure 12). It is seen that there is a clear correlation between the two quantities: the closer the O 2p-band center to

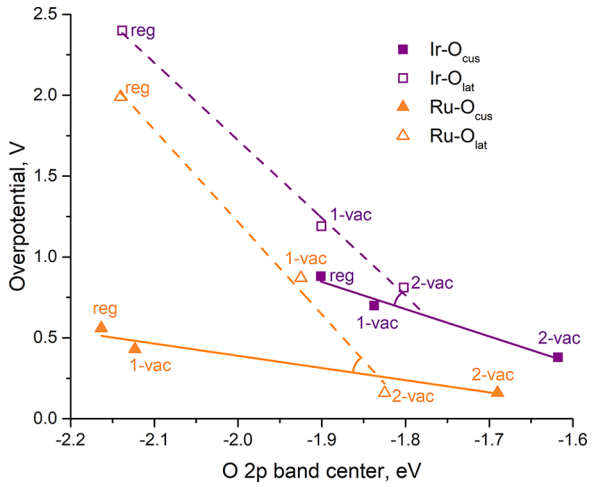


**Figure 12.** Correlation between the computed OER overpotential and O 2p-band center for the AEM (solid line) and LOM (dashed line) for the $MO_2$(110) (M = Ru, Ir) surface.

the Fermi level, the greater the OER activity. The analogous trend is observed for doped $RuO_2$ as shown in Figure S4. Moreover, we can observe that the slopes for the AEM and LOM lines are different for a given material, revealing more rapid change of $\eta_{LOM}$ upon metal-vacancy formation (see Figure 12). What is also interesting is that the LOM in $RuO_2$ turns out to be more sensitive to the formation of metal vacancies than $IrO_2$, as reflected by a larger angle between the lines for $RuO_2$ than $IrO_2$ in Figure 12. The same observation can be made when comparing the OER activity of the (211) surfaces where the LOM can outperform the AEM for $RuO_2$(211) with two metal vacancies, but not for $IrO_2$ (see Figures 8 and 9). Therefore, based on these results, we can also hypothesize that lower LOM activity of $IrO_2$ can contribute to its greater structural stability under OER conditions.

Similar electronic-structure arguments can be applied to explain the difference in reactivity between the two O sites ($O_{lat}$ and $O_{cus}$) on Ru in pure and doped $RuO_2$ by analyzing the positions of the $d_{z^2}$ and $d_{x^2-y^2}$ band centers of Ru.[50] Figure S5 shows the computed DOS projected onto the $d_{z^2}$ and $d_{x^2-y^2}$ states of Ru in pure $RuO_2$ (top panel) and 6-Ni-$RuO_2$ (bottom panel). It is seen that the $d_{z^2}$-band center is shifted to a higher energy compared to the $d_{x^2-y^2}$-band center in pure $RuO_2$, explaining a greater OER activity of $RuO_2$ via the AEM than LOM (see Figure 3a). The situation is, however, reversed for the doped system in which the $d_{x^2-y^2}$ states become closer to the Fermi level, making the LOM more preferable ($\eta_{AEM}$ = 0.88 V vs $\eta_{AEM}$ = 0.59 V for 6-Ni-$RuO_2$(110), Figure 6a).

## CONCLUSIONS

In this study, we have demonstrated that structural defects can make the lattice oxygen mechanism (LOM) competitive with the conventional adsorbate evolving mechanism (AEM) of the OER in rutile $RuO_2$ and $IrO_2$ catalysts. Specifically, we have found by considering the (110), (211), and (121) double-kink surfaces that the LOM can outperform AEM at defect sites of $RuO_2$ such as metal vacancies formed during catalyst dissolution and substitutional dopants (Ni and Co). On the example of Ni-doped $RuO_2$ with Ru vacancies, we have also revealed a synergistic effect due to the presence of both types of defects at the surface. This helps interpret why the involvement of lattice oxygen was experimentally observed for the nanocrystalline $RuO_2$-based materials, but not for the ideal metal-oxide films. $IrO_2$ is determined to be less LOM active than $RuO_2$, suggesting that the LOM should have a weaker destabilizing effect on the $IrO_2$ lattice. This could be one of the contributing factors to higher $IrO_2$ stability under electrochemical conditions. The computed projected density of states have provided insights into the differences in the local electronic structure of the AEM and LOM sites for both catalysts, indicating a clear correlation between the O 2p-band center and OER overpotential. To make this study tangible, we needed to set aside a few other aspects that can affect the interfacial behavior of rutile oxides in the OER. These include the effects of the structure and chemistry of the electrical double layer, variations in transition metal oxidation state, and OER kinetics. Future computational investigations are necessary to elucidate the role of those factors in the OER in addition to the impact of structural defects.


https://dx.doi.org/10.1021/acscatal.9b05544
ACS Catal. 2020, 10, 3650−3657

## ■ ASSOCIATED CONTENT

### Supporting Information

The Supporting Information is available free of charge at https://pubs.acs.org/doi/10.1021/acscatal.9b05544.

Additional supporting figures showing structural models and projected density of states, as well as the calculated reaction free energies with the corresponding OER overpotentials. (PDF)

## ■ AUTHOR INFORMATION


### Corresponding Author

**Vitaly Alexandrov** − *Department of Chemical and Biomolecular Engineering and Nebraska Center for Materials and Nanoscience, University of Nebraska-Lincoln, Lincoln, Nebraska 68588, United States;* orcid.org/0000-0003-2063-6914; Phone: +1 402 4725323; Email: valexandrov2@unl.edu

### Author

**Alexandra Zagalskaya** − *Department of Chemical and Biomolecular Engineering, University of Nebraska-Lincoln, Lincoln, Nebraska 68588, United States*

Complete contact information is available at: https://pubs.acs.org/10.1021/acscatal.9b05544


### Notes

The authors declare no competing financial interest.

## ■ ACKNOWLEDGMENTS

This research used resources of the National Energy Research Scientific Computing Center, a DOE Office of Science User Facility supported by the Office of Science of the U.S. Department of Energy under Contract No. DE-AC02-05CH11231. This research has been partially supported by the American Chemical Society - Petroleum Research Fund (ACS PRF 58410-DNI5).

## ■ REFERENCES


(1) Walter, M. G.; Warren, E. L.; McKone, J. R.; Boettcher, S. W.; Mi, Q.; Santori, E. A.; Lewis, N. S. Solar Water Splitting Cells. *Chem. Rev.* **2010**, *110*, 6446−6473.

(2) Cook, T. R.; Dogutan, D. K.; Reece, S. Y.; Surendranath, Y.; Teets, T. S.; Nocera, D. G. Solar Energy Supply and Storage for the Legacy and Nonlegacy Worlds. *Chem. Rev.* **2010**, *110*, 6474−6502.

(3) Katsounaros, I.; Cherevko, S.; Zeradjanin, A. R.; Mayrhofer, K. J. J. Oxygen Electrochemistry as a Cornerstone for Sustainable Energy Conversion. *Angew. Chem., Int. Ed.* **2014**, *53*, 102−121.

(4) Burke, M. S.; Enman, L. J.; Batchellor, A. S.; Zou, S.; Boettcher, S. W. Oxygen Evolution Reaction Electrocatalysis on Transition Metal Oxides and (Oxy)hydroxides: Activity Trends and Design Principles. *Chem. Mater.* **2015**, *27*, 7549−7558.

(5) Seh, Z. W.; Kibsgaard, J.; Dickens, C. F.; Chorkendorff, I.; Nørskov, J. K.; Jaramillo, T. F. Combining Theory and Experiment in Electrocatalysis: Insights into Materials Design. *Science* **2017**, *355*, eaad4998.

(6) Doyle, R. L.; Lyons, M. E. G. In *Photoelectrochemical Solar Fuel Production: From Basic Principles to Advanced Devices*; Giménez, S., Bisquert, J., Eds.; Springer International Publishing: Cham, 2016; pp 41−104.

(7) Greeley, J.; Markovic, N. M. The Road from Animal Electricity to Green Energy: Combining Experiment and Theory in Electrocatalysis. *Energy Environ. Sci.* **2012**, *5*, 9246−9256.

(8) Suen, N.-T.; Hung, S.-F.; Quan, Q.; Zhang, N.; Xu, Y.-J.; Chen, H. M. Electrocatalysis for the Oxygen Evolution Reaction: Recent Development and Future Perspectives. *Chem. Soc. Rev.* **2017**, *46*, 337−365.

(9) Cherevko, S. Stability and Dissolution of Electrocatalysts: Building the Bridge between Model and "Real World" systems. *Curr. Opin. Electrochem.* **2018**, *8*, 118−125.

(10) Geiger, S.; Kasian, O.; Ledendecker, M.; Pizzutilo, E.; Mingers, A. M.; Fu, W. T.; Diaz-Morales, O.; Li, Z.; Oellers, T.; Fruchter, L.; Ludwig, A.; Mayrhofer, K. J. J.; Koper, M. T. M.; Cherevko, S. The Stability Number as a Metric for Electrocatalyst Stability Benchmarking. *Nat. Catal.* **2018**, *1*, 508−515.

(11) Wohlfahrt-Mehrens, M.; Heitbaum, J. Oxygen Evolution on Ru and $RuO_2$ Electrodes Studied Using Isotope Labelling and On-Line Mass Spectrometry. *J. Electroanal. Chem. Interfacial Electrochem.* **1987**, *237*, 251−260.

(12) Macounova, K.; Makarova, M.; Krtil, P. Oxygen Evolution on Nanocrystalline $RuO_2$ and $Ru_{0.9}Ni_{0.1}O_{2-\delta}$ Electrodes - DEMS Approach to Reaction Mechanism Determination. *Electrochem. Commun.* **2009**, *11*, 1865−1868.

(13) Grimaud, A.; Diaz-Morales, O.; Han, B.; Hong, W. T.; Lee, Y.-L.; Giordano, L.; Stoerzinger, K. A.; Koper, M. T. M.; Shao-Horn, Y. Activating Lattice Oxygen Redox Reactions in Metal Oxides to Catalyse Oxygen Evolution. *Nat. Chem.* **2017**, *9*, 457−465.

(14) Han, B.; Grimaud, A.; Giordano, L.; Hong, W. T.; Diaz-Morales, O.; Yueh-Lin, L.; Hwang, J.; Charles, N.; Stoerzinger, K. A.; Yang, W.; Koper, M. T. M.; Shao-Horn, Y. Iron-Based Perovskites for Catalyzing Oxygen Evolution Reaction. *J. Phys. Chem. C* **2018**, *122*, 8445−8454.

(15) Shan, J.; Zheng, Y.; Shi, B.; Davey, K.; Qiao, S.-Z. Regulating Electrocatalysts via Surface and Interface Engineering for Acidic Water Electrooxidation. *ACS Energy Lett.* **2019**, *4*, 2719−2730.

(16) Yoo, J. S.; Rong, X.; Liu, Y.; Kolpak, A. M. Role of Lattice Oxygen Participation in Understanding Trends in the Oxygen Evolution Reaction on Perovskites. *ACS Catal.* **2018**, *8*, 4628−4636.

(17) Huang, Z.-F.; Song, J.; Du, Y.; Xi, S.; Dou, S.; Nsanzimana, J. M. V.; Wang, C.; Xu, Z. J.; Wang, X. Chemical and Structural Origin of Lattice Oxygen Oxidation in Co-Zn Oxyhydroxide Oxygen Evolution Electrocatalysts. *Nat. Energy* **2019**, *4*, 329−338.

(18) Stoerzinger, K. A.; Diaz-Morales, O.; Kolb, M.; Rao, R. R.; Frydendal, R.; Qiao, L.; Wang, X. R.; Halck, N. B.; Rossmeisl, J.; Hansen, H. A.; Vegge, T.; Stephens, I. E. L.; Koper, M. T. M.; Shao-Horn, Y. Orientation-Dependent Oxygen Evolution on $RuO_2$ without Lattice Exchange. *ACS Energy Lett.* **2017**, *2*, 876−881.

(19) Pavlovic, Z.; Ranjan, C.; Gao, Q.; van Gastel, M.; Schlögl, R. Probing the Structure of a Water-Oxidizing Anodic Iridium Oxide Catalyst using Raman Spectroscopy. *ACS Catal.* **2016**, *6*, 8098−8105.

(20) Kalz, K. F.; Kraehnert, R.; Dvoyashkin, M.; Dittmeyer, R.; Gläser, R.; Krewer, U.; Reuter, K.; Grunwaldt, J.-D. Future Challenges in Heterogeneous Catalysis: Understanding Catalysts under Dynamic Reaction Conditions. *ChemCatChem* **2017**, *9*, 17−29.

(21) Klyukin, K.; Zagalskaya, A.; Alexandrov, V. Ab Initio Thermodynamics of Iridium Surface Oxidation and Oxygen Evolution Reaction. *J. Phys. Chem. C* **2018**, *122*, 29350−29358.

(22) Klyukin, K.; Zagalskaya, A.; Alexandrov, V. Role of Dissolution Intermediates in Promoting Oxygen Evolution Reaction at RuO2(110) Surface. *J. Phys. Chem. C* **2019**, *123*, 22151−22157.

(23) Kasian, O.; Geiger, S.; Li, T.; Grote, J.-P.; Schweinar, K.; Zhang, S.; Scheu, C.; Raabe, D.; Cherevko, S.; Gault, B.; Mayrhofer, K. J. J. Degradation of Iridium Oxides via Oxygen Evolution from the Lattice: Correlating Atomic Scale Structure with Reaction Mechanisms. *Energy Environ. Sci.* **2019**, *12*, 3548−3555.

(24) Li, Y.-F. First-Principles Simulations for Morphology and Structural Evolutions of Catalysts in Oxygen Evolution Reaction. *ChemSusChem* **2019**, *12*, 1846−1857.

(25) Opalka, D.; Scheurer, C.; Reuter, K. Ab Initio Thermodynamics Insight into the Structural Evolution of Working $IrO_2$ Catalysts in Proton-Exchange Membrane Electrolyzers. *ACS Catal.* **2019**, *9*, 4944−4950.

(26) Schalenbach, M.; Kasian, O.; Ledendecker, M.; Speck, F. D.; Mingers, A. M.; Mayrhofer, K. J. J.; Cherevko, S. The Electrochemical

Dissolution of Noble Metals in Alkaline Media. *Electrocatalysis* **2018**, *9*, 153−161.
(27) Kresse, G.; Furthmüller, J. Efficiency of Ab-Initio Total Energy Calculations for Metals and Semiconductors Using a Plane-Wave Basis Set. *Comput. Mater. Sci.* **1996**, *6*, 15−50.
(28) Kresse, G.; Furthmüller, J. Efficient Iterative Schemes for Ab Initio Total-Energy Calculations Using a Plane-Wave Basis Set. *Phys. Rev. B* **1996**, *54*, 11169.
(29) Perdew, J. P.; Burke, K.; Ernzerhof, M. Generalized Gradient Approximation Made Simple. *Phys. Rev. Lett.* **1996**, *77*, 3865.
(30) Zhang, Y.; Yang, W. Comment on ″Generalized Gradient Approximation Made Simple″. *Phys. Rev. Lett.* **1998**, *80*, 890.
(31) Grimme, S.; Antony, J.; Ehrlich, S.; Krieg, H. A Consistent and Accurate Ab Initio Parametrization of Density Functional Dispersion Correction (DFT-D) for the 94 Elements H-Pu. *J. Chem. Phys.* **2010**, *132*, 154104.
(32) Grimme, S.; Ehrlich, S.; Goerigk, L. Effect of the Damping Function in Dispersion Corrected Density Functional Theory. *J. Comput. Chem.* **2011**, *32*, 1456−1465.
(33) Blöchl, P. E. Projector Augmented-Wave Method. *Phys. Rev. B* **1994**, *50*, 17953−17979.
(34) Kresse, G.; Joubert, D. From Ultrasoft Pseudopotentials to the Projector Augmented-Wave Method. *Phys. Rev. B* **1999**, *59*, 1758−1775.
(35) Momma, K.; Izumi, F. VESTA 3 for Three-Dimensional Visualization of Crystal, Volumetric and Morphology Data. *J. Appl. Crystallogr.* **2011**, *44*, 1272−1276.
(36) Su, J.; Ge, R.; Jiang, K.; Dong, Y.; Hao, F.; Tian, Z.; Chen, G.; Chen, L. Assembling Ultrasmall Copper-Doped Ruthenium Oxide Nanocrystals into Hollow Porous Polyhedra: Highly Robust Electrocatalysts for Oxygen Evolution in Acidic Media. *Adv. Mater.* **2018**, *30*, 1801351.
(37) Chen, S.; Huang, H.; Jiang, P.; Yang, K.; Diao, J.; Gong, S.; Liu, S.; Huang, M.; Wang, H.; Chen, Q. Mn-Doped $RuO_2$ Nanocrystals as Highly Active Electrocatalysts for Enhanced Oxygen Evolution in Acidic Media. *ACS Catal.* **2020**, *10*, 1152−1160.
(38) Matz, O.; Calatayud, M. Periodic DFT Study of Rutile IrO2: Surface Reactivity and Catechol Adsorption. *J. Phys. Chem. C* **2017**, *121*, 13135−13143.
(39) Anisimov, V. I.; Zaanen, J.; Andersen, O. K. Band Theory and Mott Insulators: Hubbard U instead of Stoner I. *Phys. Rev. B* **1991**, *44*, 943.
(40) Anisimov, V. I.; Aryasetiawan, F.; Lichtenstein, A. I. First-Principles Calculations of the Electronic Structure and Spectra of Strongly Correlated Systems: the LDA+ *U* Method. *J. Phys. Condens. Matter* **1997**, *9*, 767.
(41) Pickett, W. E.; Erwin, S. C.; Ethridge, E. C. Reformulation of the LDA+ *U* Method for a Local-Orbital Basis. *Phys. Rev. B* **1998**, *58*, 1201.
(42) Solovyev, I. V.; Dederichs, P. H.; Anisimov, V. I. Corrected Atomic Limit in the Local-Density Approximation and the Electronic Structure of *d* Impurities in Rb. *Phys. Rev. B* **1994**, *50*, 16861.
(43) Wang, L.; Maxisch, T.; Ceder, G. Oxidation Energies of Transition Metal Oxides within the GGA+ U Framework. *Phys. Rev. B* **2006**, *73*, 195107.
(44) Nørskov, J. K.; Rossmeisl, J.; Logadottir, A.; Lindqvist, L.; Kitchin, J. R.; Bligaard, T.; Jónsson, H. Origin of the Overpotential for Oxygen Reduction at a Fuel-Cell Cathode. *J. Phys. Chem. B* **2004**, *108*, 17886−17892.
(45) Man, I. C.; Su, H.-Y.; Calle-Vallejo, F.; Hansen, H. A.; Martínez, J. I.; Inoglu, N. G.; Kitchin, J.; Jaramillo, T. F.; Nørskov, J. K.; Rossmeisl, J. Universality in Oxygen Evolution Electrocatalysis on Oxide Surfaces. *ChemCatChem* **2011**, *3*, 1159−1165.
(46) Rong, X.; Parolin, J.; Kolpak, A. M. A Fundamental Relationship between Reaction Mechanism and Stability in Metal Oxide Catalysts for Oxygen Evolution. *ACS Catal.* **2016**, *6*, 1153−1158.
(47) Mathew, K.; Sundararaman, R.; Letchworth-Weaver, K.; Arias, T. A.; Hennig, R. G. Implicit solvation model for density-functional study of nanocrystal surfaces and reaction pathways. *J. Chem. Phys.* **2014**, *140*, No. 084106.
(48) Briquet, L. G. V.; Sarwar, M.; Mugo, J.; Jones, G.; Calle-Vallejo, F. A New Type of Scaling Relations to Assess the Accuracy of Computational Predictions of Catalytic Activities Applied to the Oxygen Evolution Reaction. *ChemCatChem* **2017**, *9*, 1261−1268.
(49) Gauthier, J. A.; Dickens, C. F.; Chen, L. D.; Doyle, A. D.; Nørskov, J. K. Solvation Effects for Oxygen Evolution Reaction Catalysis on IrO2(110). *J. Phys. Chem. C* **2017**, *121*, 11455−11463.
(50) Dickens, C. F.; Nørskov, J. K. A Theoretical Investigation into the Role of Surface Defects for Oxygen Evolution on RuO2. *J. Phys. Chem. C* **2017**, *121*, 18516−18524.
(51) Kasian, O.; Grote, J.-P.; Geiger, S.; Cherevko, S.; Mayrhofer, K. J. J. The Common Intermediates of Oxygen Evolution and Dissolution Reactions during Water Electrolysis on Iridium. *Angew. Chem., Int. Ed.* **2018**, *57*, 2488−2491.
(52) Wehrli, B. Monte Carlo Simulations of Surface Morphologies during Mineral Dissolution. *J. Colloid. Interface. Sci.* **1989**, *132*, 230−242.
(53) De Yoreo, J. J.; Vekilov, P. G. Principles of Crystal Nucleation and Growth. *Rev. Mineral. Geochem.* **2003**, *54*, 57−93.
(54) Stack, A. G.; Raiteri, P.; Gale, J. D. Accurate Rates of the Complex Mechanisms for Growth and Dissolution of Minerals Using a Combination of Rare-Event Theories. *J. Am. Chem. Soc.* **2012**, *134*, 11−14.
(55) Grimaud, A.; May, K. J.; Carlton, C. E.; Lee, Y.-L.; Risch, M.; Hong, W. T.; Zhou, J.; Shao-Horn, Y. Double Perovskites as a Family of Highly Active Catalysts for Oxygen Evolution in Alkaline Solution. *Nat. Commun.* **2013**, *4*, 2439.
(56) Dickens, C. F.; Montoya, J. H.; Kulkarni, A. R.; Bajdich, M.; Nørskov, J. K. An Electronic Structure Descriptor for Oxygen Reactivity at Metal and Metal-Oxide Surfaces. *Surf. Sci.* **2019**, *681*, 122−129.


https://dx.doi.org/10.1021/acscatal.9b05544
*ACS Catal.* 2020, 10, 3650−3657